remote sensing

MDPI

Article

The Climatology of Gravity Waves over the Low-Latitude Region Estimated by Multiple Meteor Radars

Jianyuan Wang [1,2,3,4], Wen Yi [3,4], Na Li [1,2], Xianghui Xue [3,4,5,6,*], Jianfei Wu [3,4], Hailun Ye [3,4], Jian Li [3,4], Tingdi Chen [3,4], Yaoyu Tian [1], Boyuan Chang [1], Zonghua Ding [1,2] and Jinsong Chen [1,2]

[1] National Key Laboratory of Electromagnetic Environment, China Research Institute of Radiowave Propagation, Qingdao 266107, China; wjy2014@mail.ustc.edu.cn (J.W.); lina861@mail.ustc.edu.cn (N.L.); tianyaoyu@pku.edu.cn (Y.T.); changyb@crirp.ac.cn (B.C.); dingzh@crirp.ac.cn (Z.D.); jschen@crirp.ac.cn (J.C.)
[2] Kunming Electro-Magnetic Environment Observation and Research Station, Qujing 655500, China
[3] CAS Key Laboratory of Geospace Environment, Department of Geophysics and Planetary Sciences, University of Science and Technology of China, Hefei 230026, China; yiwen@ustc.edu.cn (W.Y.); wujf@ustc.edu.cn (J.W.); yellen@mail.ustc.edu.cn (H.Y.); lj01511@mail.ustc.edu.cn (J.L.); chentd@ustc.edu.cn (T.C.)
[4] CAS Center for Excellence in Comparative Planetology, Anhui Mengcheng Geophysics National Observation and Research Station, University of Science and Technology of China, Hefei 230026, China
[5] Hefei National Laboratory, University of Science and Technology of China, Hefei 230026, China
[6] Collaborate Innovation Center of Astronautical Science and Technology, Harbin 150001, China
* Correspondence: xuexh@ustc.edu.cn

Abstract: Atmospheric gravity waves (GWs) can strongly modulate middle atmospheric circulation and can be a significant factor for the coupling between the lower atmosphere and the middle atmosphere. GWs are difficult to resolve in global atmospheric models due to their small scale; thus, GW observations play an important role in middle atmospheric studies. The climatology of GW variance and momentum in the low-latitude mesosphere and lower thermosphere (MLT) region are revealed using multiple meteor radars, which are located at Kunming (25.6°N, 103.8°E), Sanya (18.4°N, 109.6°E), and Fuke (19.5°N, 109.1°E). The climatology and longitudinal variations in GW momentum fluxes and variance over the low-latitude region are reported. The GWs show strong seasonal variations and can greatly control the mesospheric horizontal winds via modulation of the quasi-geostrophic balance and momentum deposition. The different GW activities between Kunming and Sanya/Fuke are possibly consistent with the unique prevailing surface winds over Kunming and the convective system over the Tibetan Plateau according to the European Centre for Medium-Range Weather Forecasts (ECMWF), Reanalysis v5 (ERA5) data, and outgoing longwave radiation (OLR) data. These findings provide insight for better understanding the coupling between the troposphere and mesosphere.

Keywords: meteor radar; gravity wave; mesospheric climatology

Citation: Wang, J.; Yi, W.; Li, N.; Xue, X.; Wu, J.; Ye, H.; Li, J.; Chen, T.; Tian, Y.; Chang, B.; et al. The Climatology of Gravity Waves over the Low-Latitude Region Estimated by Multiple Meteor Radars. *Remote Sens.* **2024**, *16*, 2870. https://doi.org/10.3390/rs16162870

Academic Editor: Silas Michaelides

Received: 14 June 2024
Revised: 26 July 2024
Accepted: 3 August 2024
Published: 6 August 2024

1. Introduction

The atmospheric gravity wave (GW) is one of the most important atmospheric waves and can alter the pattern, energetics, and dynamics of the middle atmosphere by transferring energy and momentum from the lithosphere/troposphere to the mesosphere and lower thermosphere (MLT). The GWs are excited primarily by topography, convection, wind shear, jet streams, frontal systems, and other sources in the lower atmosphere [1–3], as well as by seismic activity in the lithosphere [4,5]. The climatic anomalies and impacts of episodic events can be imprinted onto GW sources and transported to the stratosphere and/or the MLT region as the GWs propagate upward. As the GWs propagate upward, they may encounter a "critical layer", where the background wind speed is equal to the phase velocity of the GW. In this situation, the GW will break and/or dissipate, resulting in the deposition of energy and momentum into the mean flow in the MLT region [6].

This deposition of GW energy/momentum can be seen as the application of a force (often referred to as GW drag) with directions opposite to the background wind, which causes a deceleration and even a reversal of the zonal mean zonal wind in the MLT region. In addition, GWs can also induce pole-to-pole meridional circulation that leads to cold summers and warm winters in the MLT region [7] and interact with large scale waves (tides and planetary waves) [1,6,8–12]. Thus, the GW is a significant key to understanding the dynamics and thermal balances in the MLT region.

The importance of energy and momentum transfer for GWs has been well recognized [2,6,13–15]. Because of the major role of GWs in the middle atmosphere, GWs have been an essential part of global atmospheric modeling at different altitude ranges. According to the theory of GWs, the intrinsic frequency of GWs, which is observed in a frame of reference moving with the background wind, is between the buoyancy frequency and the Coriolis frequency, with a period of several minutes to several hours [1]. The horizontal wavelengths of GWs always range from approximately tens to thousands of km [1]. GWs are parameterized in global models [1,16–18], and the GW parameterization methodology requires reference to the GW spectrum, energy, and momentum [19–21]. It has also been emphasized that the parameterization of GW momentum in models should be validated using observations, which are necessary to improve GW simulations in models [17].

The GW energy and momentum are important for the understanding of middle atmospheric dynamics and energetics, which can be represented by GW variances and the vertical flux of GW momentums in observations, respectively [1,7,22–24]. A variety of instruments such as radiosondes [25–27], rocketsondes [28], radars [2,3,7,10,16,22,29–34], lidars [24,31,35–42], satellites [9,17,43–45], and airglow imagers [31,46,47], have been used to estimate the GW activity. A Fabry–Perot interferometer (FPI) can be used to invert the atmospheric wind and temperature [48,49] and is expected to be used to reflect GW activity. However, each measurement technique has its own limitations in GW observations. Radiosondes are widely used to study inertial gravity waves, but they are limited to the troposphere and lower stratosphere. The rocketsonde can provide the vertical pattern of the mesosphere, but for a short time span. Optical measurements, such as those from lidars and airglow imagers, can be used to invert atmospheric perturbations in temperature, density, and winds at high spatial and temporal resolutions, but they are easily disturbed by solar radiation, resulting in a lack of observations during the day and under cloud. Satellites such as TIMED/SABER, COSMIC, and AIRS/Aqua are extensively used to study the global variability of GWs from temperature profiles. However, these measurements can only resolve a limited spectrum of GWs due to their coarse resolution and limited spatial and temporal coverage.

Meteor radars can continuously measure neutral winds in the MLT region. According to the methodology introduced by Hocking [50], meteor radar measurements can be used to estimate GW variances and momentum fluxes in the MLT region over a long, continuous time period. Recently, this technique has been extensively used to analyze GW activity at high latitudes [16,22,51], mid-latitudes [2,3,10,52–54], and in tropical regions [15,55]. Although the climatology and latitudinal variations in GWs have been widely studied [2], comparisons of the GW climatology among locations at similar latitudes but with large topographic differences are rare. Considering the strong forcing of topography on GWs, it is necessary to analyze the impact of topographic difference on GWs propagating upward to the MLT region and the influences of these GWs on the mesospheric climate.

In this study, we present the climatology of GW variances and momentum fluxes over boreal low-latitude regions and compare the climatology of GWs over different topographies, one of which is located near the Tibetan Plateau and the other in the South China Sea. A description of the radars and methodology is presented in Section 2. The observation results regarding background winds and GWs, the interaction between GWs and background winds, and the connection between topography and MLT GWs are considered in Section 3, followed by the discussion and conclusion in Section 4.

2. Materials and Methods

2.1. Meteor Radars

The meteor radars are used to calculate the horizontal wind and GW over Kunming (25.6°N, 103.8°E), Sanya (18.4°N, 109.6°E), and Fuke (19.5°N, 109.1°E). The system parameters, geographic coordinates, and observational time periods for these meteor radars are presented in Table 1. Figure 1 presents the geographic locations of these meteor radars, where the Kunming meteor radar is located south of the Tibetan Plateau. These meteor radars are meteor detection radar (MDR) series made by ATRAD Pty Ltd., Underdale, Australia [11,56–62] and the meteor radars located at Sanya (18.4°N, 109.6°E) and Fuke (19.5°N, 109.1°E) belong to the Institute of Geology and Geophysics, Chinese Academy of Sciences (IGGCAS), which is part of the Chinese Meridian Project and the Solar–Terrestrial Environment Research Network (STERN). The Kunming meteor radar is run by Kunming Electro-magnetic Environment Observation and Research Station. After 2015, the Kunming meteor radar replaced the 53.1 MHz operating mode [63–66].

Table 1. Geographic locations, operation frequencies, and observational time periods of the meteor radars used in this study. (PRF: pulse repetition frequency).

Meteor Radar	Kunming	Kunming (after 2015)	Sanya	Fuke
Geographic Locations	25.6°N, 103.8°E	25.6°N, 103.8°E	18.4°N, 109.6°E	19.5°N, 109.1°E
Frequency	37.5 MHz	53.1 MHz	47.5 MHz	38.9 MHz
Bandwidth	75 kHz	75 kHz	75 kHz	75 kHz
Peak Power	20 kW	20 kW	20 kW	20 kW
PRF	430 Hz	430 Hz	430 Hz	430 Hz
Vertical Resolution	2 km	2 km	2 km	2 km
Data Coverage	1/1/2011–12/31/2015	1/1/2016–9/30/2020	12/1/2012–10/18/2016	1/1/2015–10/11/2019

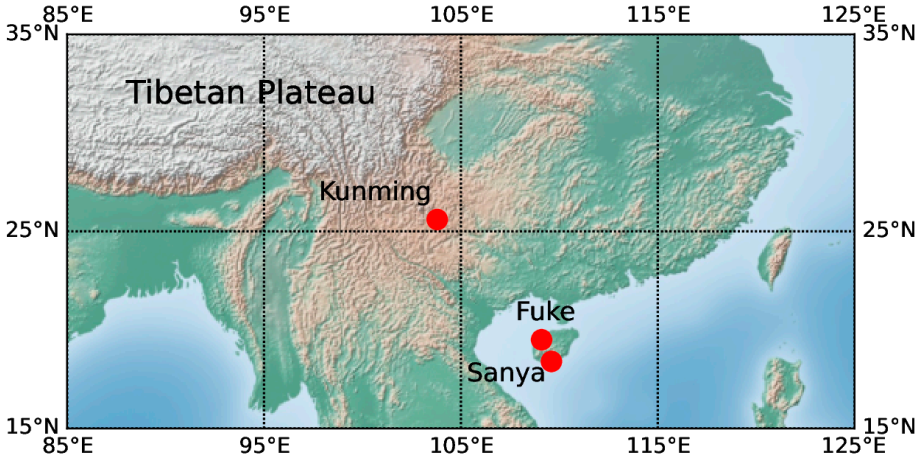

Figure 1. The topographic map around three meteor radar stations in this study. The locations of Kunming, Sanya, and Fuke are marked by red solid circles.

The radar system transmitted the radio wave and coherently detected the meteor trail reflections. The range is obtained from the time interval between transmission and detection, and the azimuth and elevation angles are calculated from the phase differences between antennas. Assuming that the vertical wind is negligible, the horizontal wind can be determined by the Doppler shift following the algorithms used in Hocking et al. [67] and Holdsworth et al. [57] Both radars are used to measure horizontal winds and GW parameters from 70 to 110 km. The temporal and altitudinal resolutions of the horizontal winds and GWs are 1 h and 2 km, respectively.

2.2. ERA5 Reanalysis

ERA5 is the fifth-generation reanalysis dataset from the ECMWF. It provides several improvements compared to ERA-I, as detailed by Hersbach and Dee [68]. The analysis is produced at a 1-hourly time step using a significantly more advanced 4D-var assimilation scheme. Its horizontal resolution is approximately 31 km, and atmospheric variables are calculated at 137 pressure levels [69]. The data for the 1979–2022 period were released in 2023. In this study, the 10 m wind in the zonal and meridional components in the single level and the monthly mean zonal and meridional winds in model levels are used to analyze the possible excitation sources of GWs.

2.3. Outgoing Longwave Radiation (OLR)

Outgoing Longwave Radiation (OLR) refers to the amount of energy emitted into space by the Earth's atmosphere, oceans, and surface. Therefore, it is a critical component of the Earth's radiation budget. In addition, OLR values are often used as a proxy for convection in tropical and subtropical regions, since cloud top temperatures (colder means higher) are an indicator of cloud height [70]. The daily OLR data are taken from twice-daily Advanced Very High Resolution Radiometer (AVHRR) soundings, with longitudinal and latitudinal grids of 2.5° × 2.5°. Usually, lower values of OLR indicate robust convective activities due to the shading of outgoing radiation by deep convective clouds [1].

2.4. Approach for Calculating the Variances and Momentum Fluxes of GWs

GWs cannot be decomposed by the observed hourly winds since the GW period is always from several minutes to hours, which is too short for the temporal resolution of horizontal winds observed by meteor radars of 1 h. To calculate the GWs from meteor radar observations, Hocking [50] proposed a new methodology for determining horizontal GW variances and the vertical fluxes of horizontal GW momentum in the zonal and meridional components, respectively. Compared to the traditional radar dual beam method [7], this method can be viewed as a generalization of the dual-beam method. The approach used to calculate GW parameters via meteor radar observations is described in Appendix A [2,32].

In this study, a 3 km altitudinal sliding window with a step of 2 km and a 2 h temporal sliding window with a step of 1 h are considered to focus on high-frequency GWs, with a period of less than 2 h, and extend the vertical range of available meteor counts to estimate reliable momentum fluxes. Only the detected meteors with zenith angles between 10° and 60° as well as radial velocities less than 200 m/s are considered, and the purpose is to remove radio echoes with large errors [2,22]. The uncertainty in estimating GW momentum fluxes primarily depends on the detected meteor counts in each altitude–time bin [23,30,32]. The simulation results of Vincent et al. [32] suggested that at least 10 meteor echoes are required in each bin to estimate credible momentum fluxes. In our analysis, the minimum of meteor counts is set to 30 in each 3 km altitudinal and 2 h temporal window to improve the precision of GW estimation. To reduce the contamination by tides, planetary waves, and prevailing winds, the modified composite day method proposed by Andrioli et al. [30] was utilized in this calculation to derive the monthly mean zonal GW momentum flux, meridional GW momentum flux, zonal GW variance, and meridional GW variance.

3. Results

3.1. Meteor Radar Observations

Before calculating the GW parameters over the low-latitude MLT region via meteor radars, it is necessary to examine the meteor echoes detected by these meteor radars. Figure 2a,b presents the meteor count rate per kilometer per hour in each altitude–time sliding window during 2011–2021 for the Kunming and Sanya/Fuke meteor radars. The empty areas indicate radar downtime or a time period without available observed data.

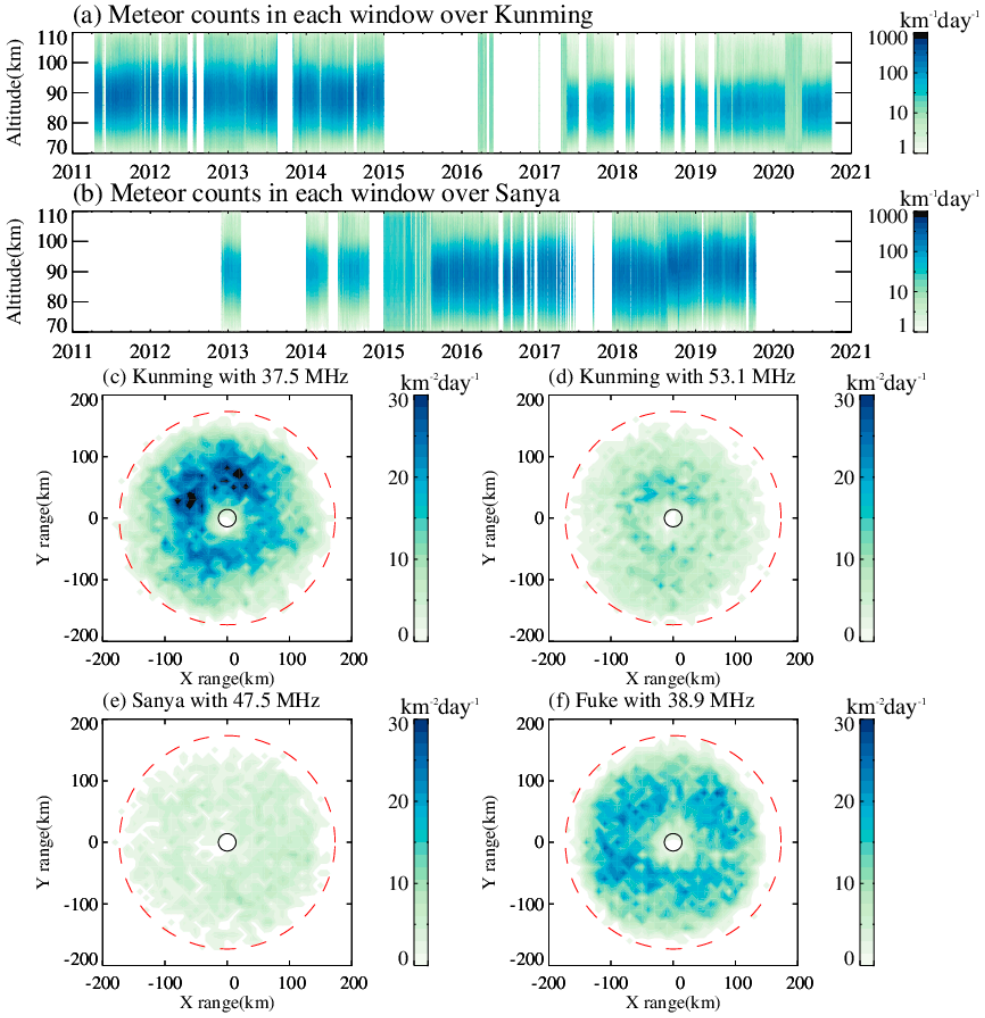

Figure 2. (**a**,**b**) The altitude–time section of meteor counts per kilometer per day throughout the time that data available over (**a**) Kunming and (**b**) Sanya in the altitude range of 70–110 km during the time period of 2011–2021. (**c**,**d**) The horizontal distribution of meteor count rates per square kilometer per day in each 10 km × 10 km bin observed by Kunming meteor radars with (**c**) 37.5 MHz and (**d**) 53.1 MHz. (**e**,**f**) As in (**c**,**d**), but observed by the Sanya and Fuke meteor radars, respectively. The black solid circle indicates a zenith angle of 10° and the red dashed circle indicates a zenith angle of 60°.

As shown in Figure 2a,b, the meteor detected echoes that primarily peaked near the altitude of 90 km. The mean meteor counts in each 3 km altitudinal and 2 h temporal window in the altitude range of 80–100 km are, respectively, ~80 and ~90 over Kunming and Sanya, and more than 85% of the meteor counts are greater than 50, which is sufficient to estimate reliable momentum fluxes. The meteor counts observed by these meteor radars show significant seasonal variation, with a maximum in boreal fall and a minimum in boreal early spring as shown in Figure A1.

However, the meteor counts are different before and after 2015 over Kunming, and this date is 21 August 2015 over Sanya, possibly due to the replacement of radar system parameters. Figure 2c–f shows the horizontal distributions of meteor-detected echoes observed by meteor radars with different operating frequencies, derived by monthly averaging in each October. The meteor echoes with zenith angles greater than 10° or less than 60° are removed in Figure 2c–f. The vast majority of meteor echoes are located within a 150 km radius around the center of the station. The normalized meteor counts are shown in Figure A2. For the Kunming radars with 37.5 MHz and 53.1 MHz, the winds observed by both meteor radars within the entire detection altitude range show strong consistency, although their operation frequencies are different (as shown in Figure A3) [63,71,72], so

that the GWs estimated by radars with different frequencies over Kunming could be jointly analyzed. Similarly, the GWs estimated by the Sanya meteor radar and Fuke meteor radar could also be jointly analyzed because of the consistency of the winds measured by the two meteor radars (as shown in Figure A3); these GWs are referred to as "GWs over Sanya/Fuke" in this study.

At the same station, the horizontal distribution of meteor positions is coherent across different radars, but the meteor counts are largely different: the meteor count rate per day observed by the Kunming meteor radar with 37.5 MHz is ~9000, and that observed by the 53.1 MHz radar is only ~3000; the meteor count rate observed by the Sanya meteor radar with 47.5 MHz is ~2500, and that observed by the Fuke meteor radar with 38.9 MHz is ~8000. Thus, priority is given to Fuke radar for the calculation of GW when there is an overlap between the observational times of the Sanya and Fuke radars.

3.2. Climatology of Horizontal Winds and GWs

Figure 3 presents the climatology of the monthly mean zonal and meridional winds as well as the GW variances in the zonal and meridional wind components between 80 and 100 km altitudes over Kunming and Sanya/Fuke. The climatology results are derived by averaging the winds and GW variances in the composite year for each month in the whole observational time period. The GW momentum fluxes, GW drag on horizontal winds, and wind tendencies (shown in Figures 4–6) were obtained via the same method.

As shown in Figure 3a,b, both zonal and meridional winds show strong seasonal variations and semiannual oscillations (SAOs), in which eastward winds prevail in May–July and December–February and southward winds prevail in February–April and August–October. Similarly, the zonal GW variance indicates a clear SAO with two peaks in April—May and August–November below 90 km. Above 90 km, the zonal GW variance is stronger in January–March and June–August, while it is weaker in October. For the meridional GW variance, the two peaks occur in February–March and September–November, which is consistent with the SAO in the southward wind. In particular, a southward wind prevails in summer (June to July) below 88 km altitude, which has a coherent manner in the enhanced meridional GW variance near 88 km in June–July. The climatology of the horizontal winds and GW variances implies that the zonal/meridional GW variances are enhanced when westward/southward winds prevail over Kunming.

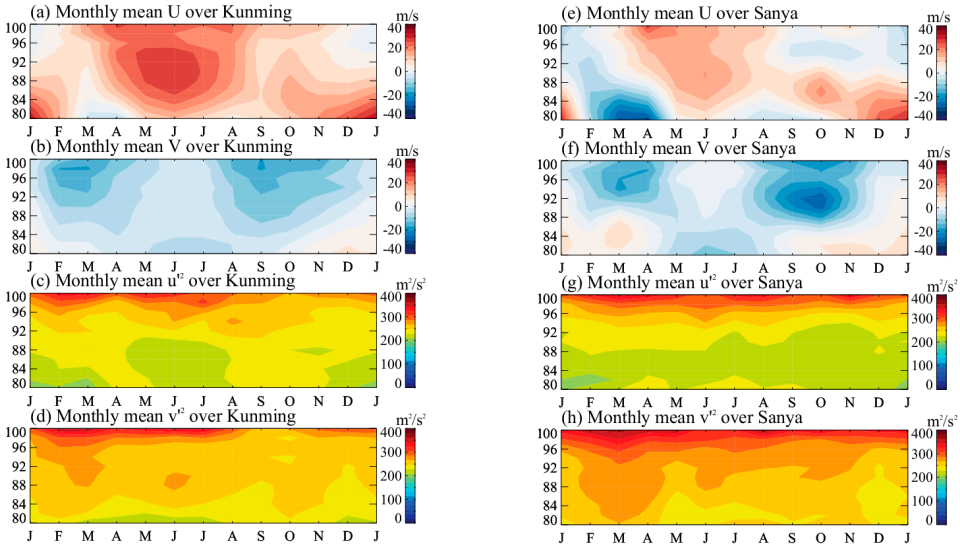

Figure 3. (**a**,**b**) The seasonal variation in the monthly mean (**a**) zonal wind and (**b**) meridional wind over Kunming in the altitude range of 80–100 km. (**c**,**d**) The seasonal variation in the monthly mean (**c**) zonal GW variance and (**d**) meridional GW variance over Kunming in the altitude range of 80–100 km. (**e**–**h**) As in (**a**–**d**), but for the observations over Sanya/Fuke. Note that the color bars are different between winds and GW variances. (U: zonal wind; V: meridional wind).

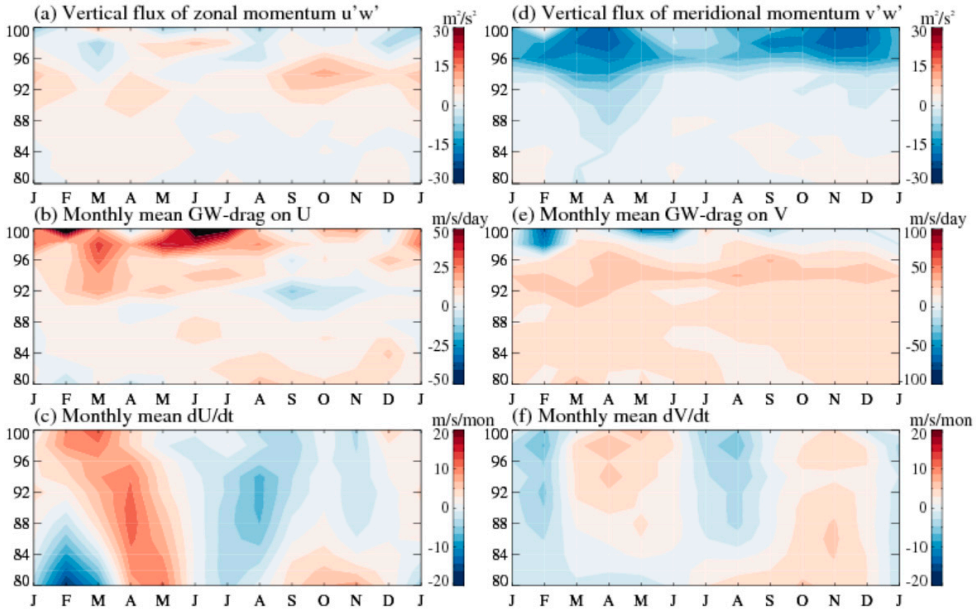

Figure 4. (**a**) The seasonal variations in the monthly mean vertical flux of zonal GW momentum over Kunming in the altitude range of 80–100 km. (**b**) The seasonal variations in the monthly mean GW drag on the zonal wind over Kunming in the altitude range of 80–100 km. (**c**) Monthly mean total zonal wind tendency over Kunming in the altitude range of 80–100 km. (**d**–**f**) As in (**a**–**c**), but for the vertical flux of meridional GW momentum, GW drag on meridional wind, and total meridional wind tendency, respectively. Note that the color bar values are different. (m/s/mon: meter per second per month).

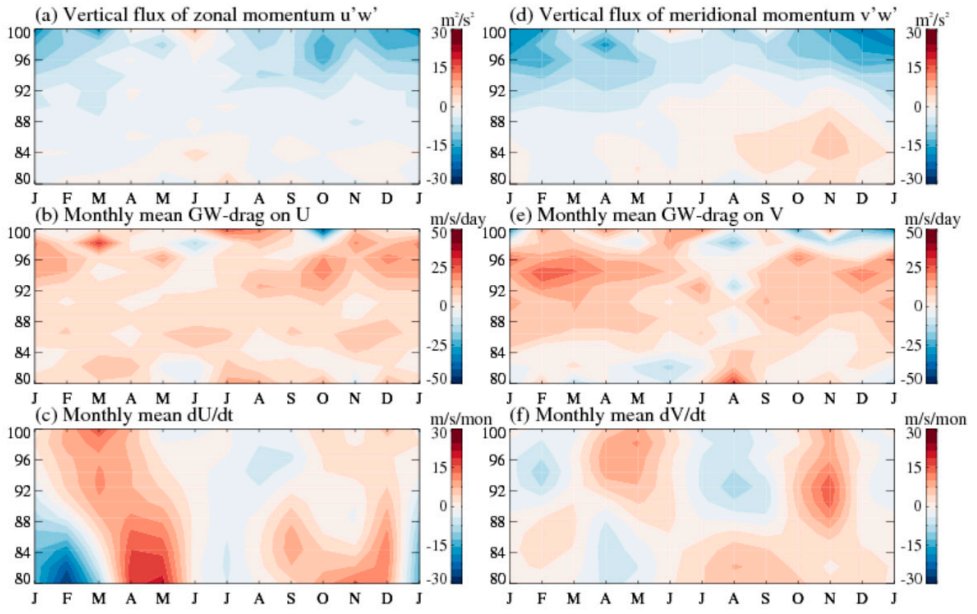

Figure 5. The same as in Figure 4, but for the results for Sanya/Fuke.

In past studies, Li et al. (2023) [73] have analyzed high-frequency (HF; GWs with timescales of 0.1–1 h in their study) and low-frequency (LF; GWs with timescales of 1–5 h in their study) GWs over Kunming, observed by the Kunming MF radar. The seasonal variations of HF GW variances in both zonal and meridional wind components in their results are slightly consistent with the zonal and meridional variances observed by Kunming meteor radars in this study. The difference between the observations via the MF radar and the meteor radar is that the maximum value of meteor radar observations is approximately 400 m^2/s^2 but the maximum of MF radar observations is ~1000 m^2/s^2,

which is more than twice that of meteor radar observations. This difference in value is possibly due to the different frequency ranges of GWs measured by the MF radar and the meteor radar [51]. Thus, the GW variances estimated by the Kunming meteor radar can reflect the GW activities in the Kunming MLT region.

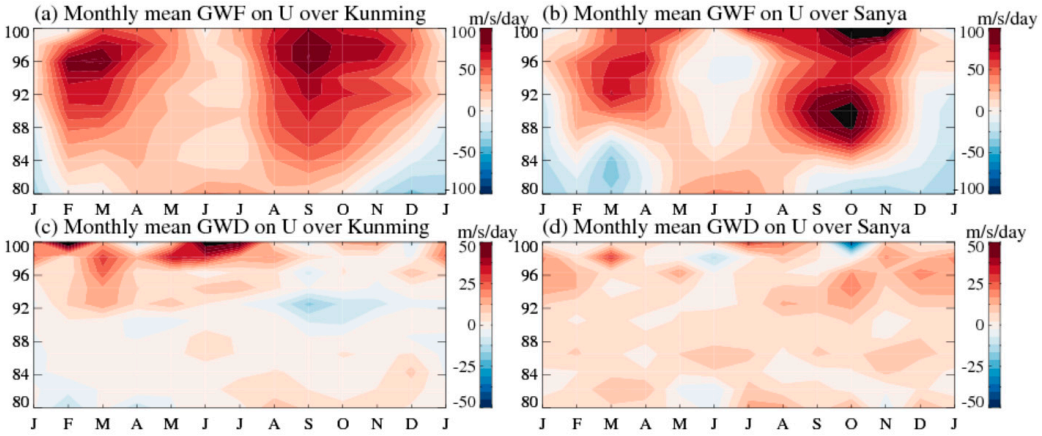

Figure 6. (**a**,**b**) Monthly mean GW forcing on zonal winds over (**a**) Kunming and (**b**) Sanya/Fuke. (**c**,**d**) The same as in (**a**,**b**), but for the GW drag on zonal winds over (**c**) Kunming and (**d**) Sanya/Fuke.

The climatology of winds and GWs over Sanya/Fuke is different from that over Kunming, even if the distance between these two stations is not as great as ~900 km. The seasonal variation in zonal winds over 90 km is primarily modulated by annual oscillation (AO), in which the eastward wind prevails in boreal spring and summer during the months of March–August and the westward wind prevails in October and January. Below 90 km altitude, a strong westward wind and another weaker westward wind occur from March to April and in August, respectively, which indicates that the AO and SAO jointly dominate the zonal flow in this altitude region. In contrast, the zonal GW variance shows few seasonal variations, with only weak SAO and two peaks in April and August. The seasonal variation in meridional winds over Sanya/Fuke is consistent with that over Kunming, and the meridional GW variance is the same.

The GWs are primarily excited by topography, convection, wind shear, jet streams, frontal systems, and other sources in the lower atmosphere [1]. The differences in atmospheric circulation between the two stations are not large, but the difference in convection and topography may cause the difference in GWs between Kunming and Sanya/Fuke. The Kunming radar station (25.6°N, 103.8°E) is located south of the Tibetan Plateau and east of the Hengduan Mountains. In the troposphere, northward–eastward winds prevail in boreal spring, summer, and winter over Kunming; the prevailing winds over Sanya/Fuke, which are consistent with the zonal mean winds, are weaker northward–eastward in the summer and southward–westward in the winter (as shown in Figure 7). Strong eastward GW momentums are excited as the prevailing eastward winds blow throughout the mountains and/or plateaus. As these eastward GW momentums break and/or dissipate in the zonal mean flow and deposit eastward momentum in the zonal mean flow, the eastward wind over Kunming in the MLT altitude region is greater than that over Sanya/Fuke at the same altitude in summer and winter.

3.3. Interaction between Horizontal Winds and GWs

Since the background wind can selectively filter GWs in specific directions [6], the horizontal propagation directions and momentums of GWs are important for the horizontal wind in the middle atmosphere. Figure 4a,d shows the seasonal variations in the vertical fluxes of zonal and meridional momentum, respectively, over Kunming in the altitude range of 80–100 km.

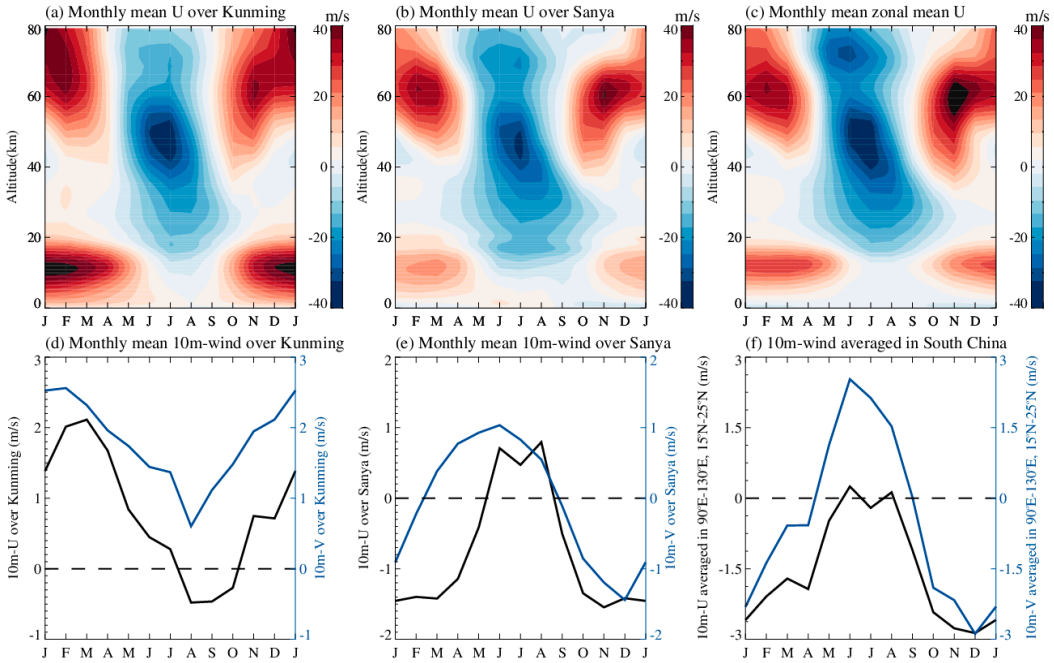

Figure 7. (**a**–**c**) Month–altitude sections of the monthly mean zonal winds over (**a**) Kunming and (**b**) Sanya, and (**c**) the monthly mean zonal mean zonal winds derived from the ERA5 reanalysis in the altitude range of 0–80 km. (**d**–**f**) The monthly mean 10 m zonal wind (black solid line) and meridional wind (blue solid line) over (**d**) Kunming and (**e**) Sanya, and (**f**) averaged in 90°E–130°E and 15°N–25°N, derived from the ERA5 reanalysis data. The black dashed lines indicate a wind velocity of zero.

As shown in Figure 4a,d, the zonal and meridional GW momentums both show strong SAOs, in which the GW momentums strongly propagate eastward in February–May and September–November, and propagate southward in February–May and October–December. The prevailing direction of zonal/meridional GW momentums is always opposite to the prevailing direction of zonal/meridional background winds that are not inverted at altitude; for the zonal/meridional background winds inverted at altitude, the direction of GW momentums is consistent with the direction of the winds at higher altitudes. This phenomenon is possibly due to the interaction of the zonal flow and the zonal GW momentum [6].

As westward winds prevail over Kunming below the mesopause (by ~90 km), the GWs propagating westward are filtered and more GWs propagating eastward are induced to propagate upward. When the eastward GWs dissipate by breaking in the mesopause, the eastward momentum is deposited into the background wind until the wind is reversed into an eastward wind, and a weaker eastward-propagating GW is excited secondarily above the mesopause.

For the meridional winds and GWs, the situation is much the same as that for the zonal winds and GWs. In contrast, the meridional winds below ~84 km are northward in winter and southward in summer, while the GWs below ~88 km propagate southward in March–June and northward in August–February. This climatology of meridional winds is referred to as pole-to-pole residual circulation, which is derived from the meridional GW momentum forcing in the mesosphere. The GW momentum forcing, referred to as GW drag on horizontal winds (GWD), can be calculated via the vertical fluxes of horizontal GW momentum [1,74], which is given as

$$\left(GWD_x, GWD_y\right) \triangleq -\frac{\partial\left(\overline{u'w'}, \overline{v'w'}\right)}{\partial z}, \quad (1)$$

where GWD represents the GW drag on horizontal winds. The central difference is applied to calculate the GWD via the $u'w'$ and $v'w'$ estimated by meteor radars.

Figure 4b,e presents the monthly mean GW drag on zonal and meridional winds calculated by Kunming meteor radar observations in the altitude range of 80–100 km; the monthly mean zonal and meridional wind tendencies in the same altitude range are shown in Figure 4c,f. In the zonal wind component, the zonal GWD is westward in the late summer/fall and winter, which is partially consistent with the zonal wind tendency. The others' variabilities in zonal GWD are different from those with zonal wind tendency, and the zonal GWD is weaker than the zonal wind tendency, implying that the climatology of zonal winds could also be modulated by the GWs not observed by meteor radars and/or other dynamic processes.

For the meridional wind component, the meridional GWD is northward in March–May and September–December and southward in January–February and March–July above ~96 km, which is consistent with the meridional wind tendency. This result suggests that the SAO can be derived well from the GWs observed by the Kunming meteor radar. The meridional GWD does not show the features that drive the meridional residual circulation because the altitude range of the wave sources of the meridional residual circulation is ~80 km, which is not included in the meteor radar observations due to fewer meteor counts at this altitude. Nevertheless, the meridional GW momentum also shows that the GWs propagate southward in the spring/summer and northward in the fall/winter, which implies that the GW exerts forces on the pole-to-pole residual circulation.

Figure 5 presents the GW momentum, GWD, and horizontal wind tendency observed by the Sanya and Fuke meteor radars. In contrast to the zonal GW momentums over Kunming, the zonal GW momentums over Sanya/Fuke show a strong AO, in which the zonal momentum is eastward in summer and westward in winter. The westward momentum is rapidly enhanced with increasing altitude from August to May, and the eastward momentum in summer is slightly reduced at ~92 km and resumed above that altitude. The altitudinal variability of zonal GW momentums suggests that the zonal GWD will usually be eastward and will be slightly westward only in summer (by ~June–July), as shown in Figure 5b. Compared to the zonal wind tendency over Sanya/Fuke (as shown in Figure 5c), the zonal GWD estimated by the Sanya and Fuke meteor radars can explain why the AO is above 90 km, the zonal wind is eastward in spring and summer, and the zonal wind is westward in fall and winter. The GWDs driving the SAO are at lower altitudes, so they cannot be calculated by meteor radars.

Figure 5d shows the meridional GW momentum estimated by the Sanya and Fuke meteor radars. The meridional GW momentum shows a strong AO below 90 km, in which the meridional momentum is southward from February to June and northward from July to January, and an SAO above 90 km, in which the southward momentum prevails throughout the year and has two peaks in spring and late fall. The meridional GWD derived from meridional GW momentum (as shown in Figure 5e) shows that the AO is below 86 km, that the GWD is southward from April to June, northward in other months, and shows a strong SAO at higher altitudes, that the meridional GWD is northward in spring and fall, and that the GWD is southward in August and December/January. Compared to the meridional wind tendency (as shown in Figure 5f), the meridional GWD shows strong consistency with the meridional wind tendency, indicating that the climatology of meridional wind over Sanya/Fuke primarily results from GW forcing.

Interestingly, compared with past studies on GWs over the boreal MLT region near 120°E [2,3,75,76], the climatology of meridional GW momentum over Sanya/Fuke shows strong consistency with the results over Mohe, Beijing, Mengcheng, and Wuhan [2]. In addition, the meridional wind over Sanya/Fuke is also consistent with the meridional wind observed by those radars. This phenomenon implies that the meridional winds observed by these radars located at different latitudes are all modulated by the same meridional circulation, which is forced by GWs varying with the same seasonal variation. The meridional GW momentum over Kunming is slightly different from that observed by

the radars located near 120°E, possibly due to the topographic difference between Kunming and other locations.

The climatology of the GW momentum direction over Sanya/Fuke, which is northeastward in summer and south-westward in winter, is consistent with that in several Northern Hemisphere observations [47,77]. In past studies, the unique propagation direction of GWs near Kunming observed by other measurements, such as airglow imager [78], has been reported. In this study, the GW momentums over Kunming below 90 km are eastward and southward in spring and winter, while GW momentums are eastward and northward in summer and fall, respectively. Li et al. [78] have analyzed the GWs over Qujing (25.6°N, 103.7°E) observed by an airglow imager, and they reported that GWs propagate eastward and southward in winter, but eastward and northward in spring, summer, and fall. Although the meridional direction differs between these two results, the seasonal variation in the zonal direction of GW momentum observed by the Kunming meteor radar in this study is consistent with the zonal propagation direction of GW observed by the Qujing airglow imager. The possible sources, due to the unique directions of GW momentum over Kunming, will be considered in Section 3.4.

For zonal wind, Ma et al. [75] have estimated GW forcing on mean flow (GWF) via mean zonal wind and mean meridional wind using the methodology proposed by Liu et al. [79], but their study has not considered comparing the GWF and GWD estimated by meteor radars. The zonal mean GWF can be expressed as [79]

$$\frac{Du}{Dt} = \left(f + \frac{\overline{u}tan\varphi}{a}\right)\overline{v} + \overline{GWF}, \tag{2}$$

where f is the Coriolis parameter; $\overline{u}$ and $\overline{v}$ represent the zonal mean zonal wind and zonal mean meridional wind, respectively; φ is the latitude; and a is the Earth radius. With the assumption that Du/Dt is much smaller than the zonal mean GWF, the simple force balance is given as [75,79]

$$\overline{GWF} \triangleq -\left(f + \frac{\overline{u}tan\varphi}{a}\right)\overline{v}, \tag{3}$$

in this study, $\overline{u}$ and $\overline{v}$ are replaced by the monthly mean zonal and meridional winds to calculate the GWF over Kunming and Sanya/Fuke.

Figure 6 shows a comparison of the GWF and GWD over Kunming and Sanya/Fuke. According to the Sanya and Fuke radar observations, the seasonal variation in the monthly mean GWF is largely coherent with the seasonal variation in the monthly mean zonal GWD, despite the differences in their magnitudes. This result indicates that the vertical gradient of zonal GW momentum is approximately equal to the Coriolis forcing on the zonal mean zonal wind. This finding implies that the GWD over Sanya/Fuke is approximately consistent with the "normal" GWD. However, this situation is different over Kunming. The GWD over Kunming is almost opposite to the GWF over Kunming in spring and summer in the altitude range of ~88–94 km, although the GWF over Kunming is consistent with the GWF over Sanya/Fuke. Interestingly, the part of the Kunming GWD that differs from the GWF is associated with the zonal wind tendency over Kunming, possibly meaning that the "anomalous" Kunming GWD (the difference between Kunming GWD and "normal" GWD) results in the localized zonal wind tendency in the Kunming MLT region. This "anomalous" Kunming GWD may be excited by the unique topography and/or prevailing tropospheric winds near Kunming.

3.4. Possible Sources of Anomalous GWs over Kunming

Several factors can affect the direction of GW momentum, including the GW sources and the critical layer wind-filtering effect.

Figure 7a–c presents the monthly mean zonal winds over Kunming and Sanya/Fuke and the monthly mean zonal mean zonal winds averaged in 15°N–25°N, derived from the ERA5 reanalysis in the altitude range of 0–80 km. These background winds exhibit

the same seasonal pattern: westward winds prevail in summer from ground to ~80 km and eastward winds prevail in winter in the altitude ranges of ~0–20 km and ~40–80 km. The climatology of the mean flow can explain the "normal" seasonal variation in GWs in the Northern Hemisphere, in that the directions of GW momentum are always opposite to the direction of background winds induced by the critical layer wind-filtering effect. However, the background wind filtering cannot play a dominant role in driving the unique directions of GWs over Kunming because the background winds below the MLT region are not significantly different from the zonal mean flow.

As discussed above, the "anomalous" GW activity over Kunming is possibly due to the unique topography and/or prevailing tropospheric winds near Kunming, which excite unique GWs, and these GWs propagate upward to the MLT region. However, the horizontal scale of orographic gravity waves is always short by tens of kilometers [1], which is difficult to resolve in most atmospheric models and is rarely to be observed. Considering the excitation process of the orographic waves, the surface winds could be associated with the orographic waves [80].

Figure 7d–f shows the monthly mean 10 m zonal winds and 10 m meridional winds over Kunming and Sanya, respectively, averaged in 90°E–130°E and 15°N–25°N, derived from the ERA5 reanalysis data. The 10 m zonal winds and 10 m meridional winds over Sanya are consistent with the averaged 10 m winds, which are north-eastward in summer and south-westward in winter. Interestingly, both the 10 m zonal wind and 10 m meridional wind over Kunming are greatly different from those over Sanya and are averaged across south China. The 10 m meridional wind over Kunming prevails southward during the whole year and reaches a minimum in August; the 10 m zonal wind is eastward in spring, summer, and winter, and westward in fall. According to the theory of excitation of orographic waves, these unique surface winds will excite the GWs, with the momentum in the same direction as the surface winds when the stably stratified airflow moves over mountains. These orographic wave momentums can propagate vertically upward to the MLT region due to their phase speeds being near zero. This process may be a factor that leads to the unique GW momentums over Kunming.

In addition, tropospheric convection [1,81] is also an important source of GWs. In contrast to orographic waves, the convective GWs can propagate both vertically and horizontally. Because the horizontal pattern of GWs cannot be provided by a single meteor radar, it is difficult to determine the locations of GW sources. Thus, the consideration of the role of convective systems in the GWs will be only a wide and cursory discussion.

Usually, lower values of OLR indicate infrared emissions from deep convective clouds with robust convective activities. Figure 8 presents the OLR data in the longitudinal and latitudinal ranges of 65°E–125°E and 15°N–45°N during spring, summer, fall, and winter, respectively. As shown in Figure 8, the convective activities over Kunming are primarily controlled by the Tibetan Plateau and Indian Ocean, in which the convection is strongly forced by the convective system over the Tibetan Plateau during spring and winter, and is modulated by the convective clouds from both the Tibetan Plateau and Indian Ocean during summer and fall. The OLRs over Kunming and Sanya, which represent infrared emissions from deep convective clouds, are lower in the spring and reach their minimum values in the summer, indicating the enhancement of convection.

The GWs can be generated by a strong convective system and propagate upward after being selectively filtered by the mean flow. In boreal winter and spring, the convection over south China is primarily controlled by the convective system over the Tibetan Plateau, which is located northwest of Kunming and Sanya. In the stratosphere, the zonal wind is eastward (as shown in Figure 7), so only the GWs propagating westward and the GWs propagating eastward with slow zonal phase speeds can reach the upper altitude region. Considering the relative location of the convective source, the propagation direction of GWs over Kunming will be eastward and these GWs will not occur over Sanya due to the excessive distance between the convective source and Sanya. In the summer, the south China region is controlled by a strong convective system from the Indian Ocean,

which is located southwest of Kunming and Sanya. The westward prevailing wind in the stratosphere has difficulty filtering the GWs propagating eastward; thus, the propagation directions of GWs over Kunming and Sanya are both eastward in the summer.

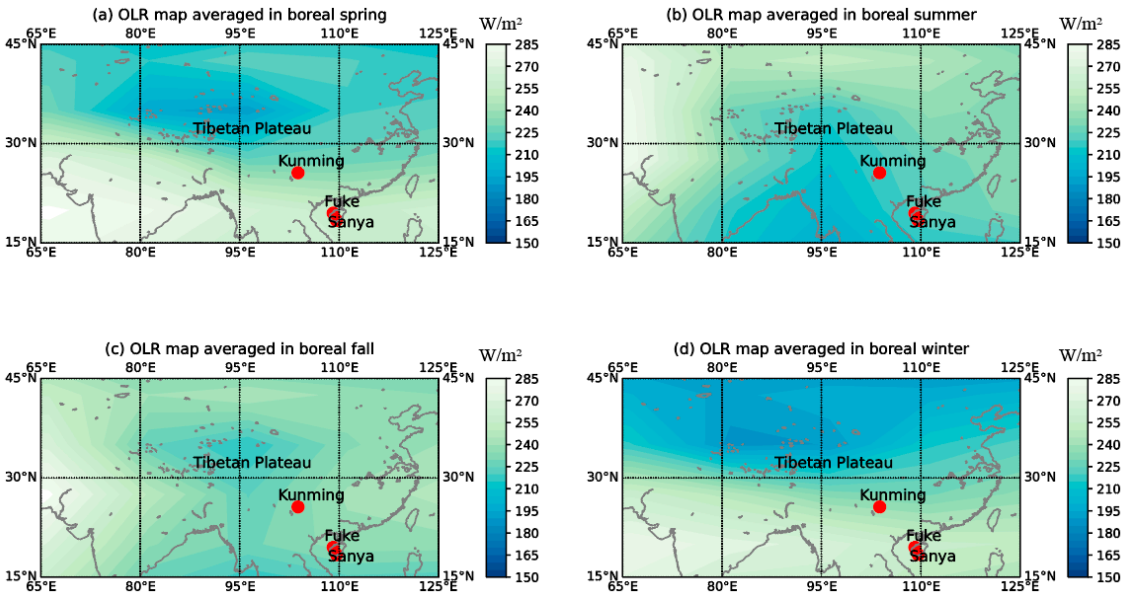

Figure 8. Distributions of OLR data observed by AVHRR soundings in the longitudinal and latitudinal range of 65°E–125°E and 15°N–45°N during (**a**) March–April–May, (**b**) June–July–August, (**c**) September–October–November, and (**d**) December–January–February, respectively.

4. Discussion and Conclusions

The GW momentum fluxes and variances over the low-latitude MLT region are investigated using multiple meteor radar observations. The GW activities are strong over Kunming and Sanya/Fuke, with GW variances of ~200–400 m^2/s^2. The magnitudes of the vertical fluxes of GW momentums are ~1–20 m^2/s^2 and ~1–15 m^2/s^2 over Kunming and Sanya/Fuke, respectively. The GW drag on horizontal winds is estimated by the vertical gradient of the momentum fluxes, with values ranging from approximately −75 m/s/day to 50 m/s/day.

Radar observations at some sites have been used to estimate GW momentum fluxes and GW drags in the MLT region. At tropical stations, the momentum fluxes of ~2–8 m^2/s^2 over Jicamarca (12°S) [82] and ~1–15 m^2/s^2 at three tropical stations [14] were observed, with GW drags of ~10–60 m/s/day. At extratropical stations, mean values of momentum fluxes of ~1–10 m^2/s^2 have been reported, with the GW drags in the range of ~10–70 m/s/day [83]. Jia et al. [2] have compared some of the observations over the mid-latitude region, and the momentum fluxes are highly variable, with peak values of ~4–20 m^2/s^2. Compared to other meteor radar observations, the magnitudes of momentum fluxes and GW drags are of the same order as other observations worldwide.

The climatology of the GWs over the low-latitude MLT region is analyzed in this study. The zonal GW variances over Kunming below ~90 km altitude reach two peaks in spring and fall, but the seasonal variation in the zonal GW variances over Sanya/Fuke is much weaker. The meridional variances over Kunming and Sanya/Fuke show similar seasonal variations, which have two peaks in February–March and September–November. These SAO-like variabilities in GWs below ~90 km altitude may be due to the critical layer wind-filtering effect of SAO in the upper stratosphere on GWs with upward propagation.

The momentum fluxes over Kunming and Sanya/Fuke both show semiannual variability above 90 km and annual variability below 90 km. The SAO-like variability in the GWs above 90 km could be consistent with the interaction between the winds at ~90 km and the GWs. The GW-induced forces on horizontal winds (referred to as GWD in this

study) are estimated by the vertical gradient of momentum fluxes in this study. It is shown that the semiannual variability in the meridional GWD is consistent with that in the SAO under winds in the same direction. Although the seasonal variation in the zonal GWD is different from the zonal wind tendency, the zonal GWD over Sanya/Fuke is in balance with the Coriolis term, implying that the zonal wind is forced by the zonal GWD by modulating the geostrophic/quasi-geostrophic balance. The zonal GWD over Kunming shows less correlation with both the zonal wind tendency and the Coriolis term, possibly due to the unique wave sources near Kunming.

The momentum fluxes over Kunming and Sanya/Fuke below 90 km altitude show different seasonal variations. The GW momentum direction over Sanya/Fuke is northeastward in the summer and south-westward in the winter, which is consistent with several observations in east Asia [2,47,77,78]. However, the zonal GW momentum over Kunming is eastward throughout the year, and the meridional momentum is southward in spring and winter, and northward in summer and fall. This difference is considered to be related to the unique tropospheric prevailing winds near Kunming and the convective system over the Tibetan Plateau according to the ERA5 reanalysis and OLR data.

In conclusion, the results can be summarized as follows:

(1) The GW variances and momentum fluxes over the low-latitude MLT region can be estimated by multiple meteor radars. These radars are located at Kunming, Sanya, and Fuke. The GW variances over Kunming and Sanya/Fuke both show semiannual variability below 90 km and annual variability above 90 km, which is consistent with the seasonal variation in background winds.
(2) The vertical fluxes of GW momentum in both the zonal and meridional wind components differ between Kunming and Sanya/Fuke. According to the interaction between GWs and background winds, these longitudinal differences in GW momentum could be considered to be one of the causes of the differences in the climatology of background winds between Kunming and Sanya/Fuke by modulating the quasi-geostrophic balance and the momentum deposition.
(3) The different GW activities between Kunming and Sanya/Fuke are possibly consistent with the unique prevailing surface winds over Kunming and the convective system over the Tibetan Plateau, according to the ERA5 reanalysis data and the OLR data.

These results indicate that the GWs can greatly modulate middle-atmospheric dynamics and that these waves are primarily controlled by the lower atmosphere and small-scale variability. To our knowledge, this is the first time that the longitudinal difference in the MLT background wind via the GW activities has been explained, and that the impact of the topographic and convective differences on GWs has been considered. In this situation, the GWs can be a significant key for understanding the coupling between tropospheric climate and middle-atmospheric dynamics. Considering that small-scale GWs are difficult to resolve in current models, these findings provide insight into GW activities over the low-latitude region, and will contribute to global circulation models.

Author Contributions: Conceptualization, J.W. (Jianyuan Wang) and X.X.; methodology, J.W. (Jianyuan Wang), W.Y., H.Y. and X.X.; software, J.W. (Jianyuan Wang), Y.T., B.C. and J.W. (Jianfei Wu); validation, X.X., W.Y. and N.L.; formal analysis, J.W. (Jianyuan Wang), W.Y. and X.X.; investigation, J.W. (Jianyuan Wang) and J.L.; resources, X.X. and N.L.; data curation, T.C. and J.C.; writing—original draft preparation, J.W. (Jianyuan Wang); writing—review and editing, J.W. (Jianyuan Wang), X.X. and W.Y.; visualization, J.W. (Jianyuan Wang); supervision, X.X. and W.Y.; project administration, X.X., W.Y. and N.L.; funding acquisition, Z.D., X.X. and W.Y. All authors have read and agreed to the published version of the manuscript.

Funding: This work is supported by the National Key R&D Program of China (Grant No. 2022YFF0503704), National Natural Science Foundation of China (42125402 and 42174183), the Wei Fengsi Academician's Studio Fund (Grant No. A392401008), and the National Key Laboratory of Electromagnetic Environment Fund under the Grant No. 6142403230105.

Data Availability Statement: The Sanya meteor radar data are available from the website of the world data center for Geophysics, Beijing: http://wdc.geophys.ac.cn/index.asp (accessed on 1 June 2020). The Kunming meteor radar data are available from https://doi.org/10.5281/zenodo.10829069 (accessed on 20 March 2024). The ERA5 reanalysis dataset are available from https://cds.climate.copernicus.eu/ (accessed on 4 June 2024). The outgoing longwave radiations are available from https://doi.org/10.7289/V5SJ1HH2 (accessed on 1 January 2022).

Acknowledgments: We acknowledge the use of data from the Chinese Meridian Project (www.meridianproject.ac.cn, accessed on 4 June 2024). We acknowledge the data resources from the National Space Science Data Center, National Science & Technology Infrastructure of China. (https://www.nssdc.ac.cn, accessed on 4 June 2024).

Conflicts of Interest: The authors declare no conflicts of interest.

Appendix A

In general, the meteor radar is used to measure the meteor locations (zenith angle, azimuth angle, and range) and radial velocity by utilizing the radio reflections from the meteor trails in the MLT region. The radial velocities are clustered into specific altitude and time windows, usually set at 1 h and 2 km to ensure that a sufficient number of meteors are observed in each window. The horizontal winds can be estimated via using least square fits to the all-sky radial velocities in each altitude–time window, which is as follows [2]

$$v_{rad} = Usin\theta cos\phi + Vsin\theta sin\phi + Wcos\theta + residual, \quad (A1)$$

where v_{rad} represents the radial velocity; U represents the mean zonal wind; V represents the mean meridional wind; W represents the mean vertical wind; θ and ϕ represent the zenith angle and azimuth, respectively.

To analyze the residual of radial velocity, the mean winds are used to calculate the mean radial velocity v_{radm}, which is written as

$$v_{radm} = Usin\theta cos\phi + Vsin\theta sin\phi + Wcos\theta, \quad (A2)$$

and the residual is given by

$$\sum {v'_{rad}}^2 = \sum (v_{rad} - v_{radm})^2, \quad (A3)$$

where $v'_{rad} = v_{rad} - v_{radm}$ represents the residual of radial velocity.

It is assumed that the neutral wind is uniform over all the detected positions in each window in Equation (A1). However, the observed winds are not uniform, and the observed radial velocity usually differs from the value of mean radial velocity. These differences can be attributed to the effect of atmospheric waves on the neutral winds. The dominant waves in the MLT region are GWs, tides, and planetary waves, in which the period of planetary waves is longer than one day and the period of tides is always longer than several hours. To estimate the effect of GWs, the time and altitude windows are set as 2 h and 2 km, respectively. Assuming the differences in the radial velocities in each 2 h–2 km window are mainly due to gravity waves, an all-sky fit of the square of residual of radial velocity is performed as

$$v'_{rad} = u'sin\theta cos\phi + v'sin\theta sin\phi + w'cos\theta + residual, \quad (A4)$$

and the residual is given by

$$\Lambda = \sum \left[{v'_{rad}}^2 - \left(u'sin\theta cos\phi + v'sin\theta sin\phi + w'cos\theta \right)^2 \right]^2, \quad (A5)$$

where u', v', and w' represent the perturbations of zonal wind, meridional wind, and vertical wind, respectively. Λ represents the sum of squares of the residual of all-sky radial velocity perturbations due to GWs in each window.

To minimize Λ, the Equation (A5) has been partially differentiated with respect to each perturbation term, and then it is obtained as

$$2\sum[{v'_{rad}}^2 - (u'^2 sin^2\theta cos^2\phi + v'^2 sin^2\theta sin^2\phi + w'^2 cos^2\theta + 2u'v' sin^2\theta cos\phi sin\phi + 2u'w' sin\theta cos\theta cos\phi + 2v'w' sin\theta cos\theta sin\phi))]sin^2\theta cos^2\phi = 0, \quad \text{(A6)}$$

where u'^2, v'^2, w'^2 indicate the GW variance in zonal, meridional, and vertical components, respectively; $u'w'$ and $v'w'$ indicate the vertical fluxes of zonal and meridional GW momentum, respectively. The parameters u'^2, v'^2, w'^2, $u'v'$, $u'w'$, and $v'w'$ are all assumed to be uniform over the observational region.

The matrix forms of Equation (A6) can be written as

$$\begin{bmatrix} \sum sin^4\theta cos^4\phi & \sum sin^4\theta cos^2\phi sin^2\phi & \sum sin^2\theta cos^2\theta cos^2\phi & 2\sum sin^4\theta cos^3\phi sin\phi & 2\sum sin^3\theta cos\theta cos^3\phi & 2\sum sin^3\theta cos\theta sin\phi cos^2\phi \\ \sum sin^4\theta sin^2\phi cos^2\phi & \sum sin^4\theta sin^4\phi & \sum sin^2\theta cos^2\theta sin^2\phi & 2\sum sin^4\theta sin^3\phi cos\phi & 2\sum sin^3\theta cos\theta sin^2\phi cos\phi & 2\sum sin^3\theta cos\theta sin^3\phi \\ \sum sin^2\theta cos^2\theta cos^2\phi & \sum sin^2\theta cos^2\theta sin^2\phi & \sum cos^4\theta & 2\sum sin^2\theta cos^2\theta sin\phi cos\phi & 2\sum sin\theta cos^3\theta cos\phi & 2\sum sin\theta cos^3\theta sin\phi \\ 2\sum sin^4\theta cos^3\phi sin\phi & 2\sum sin^4\theta sin^3\phi cos\phi & 2\sum sin^2\theta cos^2\theta sin\phi cos\phi & 4\sum sin^4\theta sin^2\phi cos^2\phi & 4\sum sin^3\theta cos\theta sin\phi cos^2\phi & 4\sum sin^3\theta cos\theta sin^2\phi cos\phi \\ 2\sum sin^3\theta cos\theta cos^3\phi & 2\sum sin^3\theta cos\theta sin^2\phi cos\phi & 2\sum sin\theta cos^3\theta cos\phi & 4\sum sin^3\theta cos\theta sin\phi cos^2\phi & 4\sum sin^2\theta cos^2\theta cos^2\phi & 4\sum sin^2\theta cos^2\theta sin\phi cos\phi \\ 2\sum sin^3\theta cos\theta sin\phi cos^2\phi & 2\sum sin^3\theta cos\theta sin^3\phi & 2\sum sin\theta cos^3\theta sin\phi & 4\sum sin^3\theta cos\theta sin^2\phi cos\phi & 4\sum sin^2\theta cos^2\theta sin\phi cos\phi & 4\sum sin^2\theta cos^2\theta sin^2\phi \end{bmatrix}$$

$$\begin{bmatrix} u'^2 \\ v'^2 \\ w'^2 \\ u'v' \\ u'w' \\ v'w' \end{bmatrix} = \begin{bmatrix} \sum {v'_{rad}}^2 sin^2\theta cos^2\phi \\ \sum {v'_{rad}}^2 sin^2\theta sin^2\phi \\ \sum {v'_{rad}}^2 cos^2\theta \\ 2\sum {v'_{rad}}^2 sin^2\theta sin\phi cos\phi \\ 2\sum {v'_{rad}}^2 sin\theta cos\theta cos\phi \\ 2\sum {v'_{rad}}^2 sin\theta cos\theta sin\phi \end{bmatrix} \quad \text{(A7)}$$

Appendix B

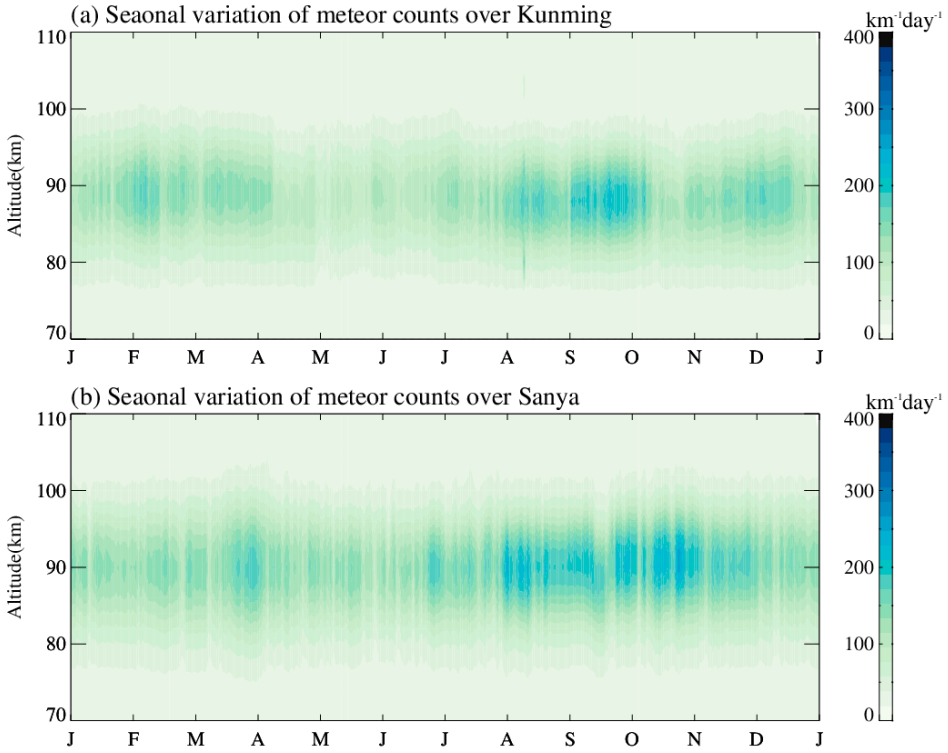

Figure A1. The seasonal variation of meteor counts per kilometer per day throughout the time that data were available over (**a**) Kunming and (**b**) Sanya, in the altitude range of 70–110 km during the time period of 2011–2021, respectively.

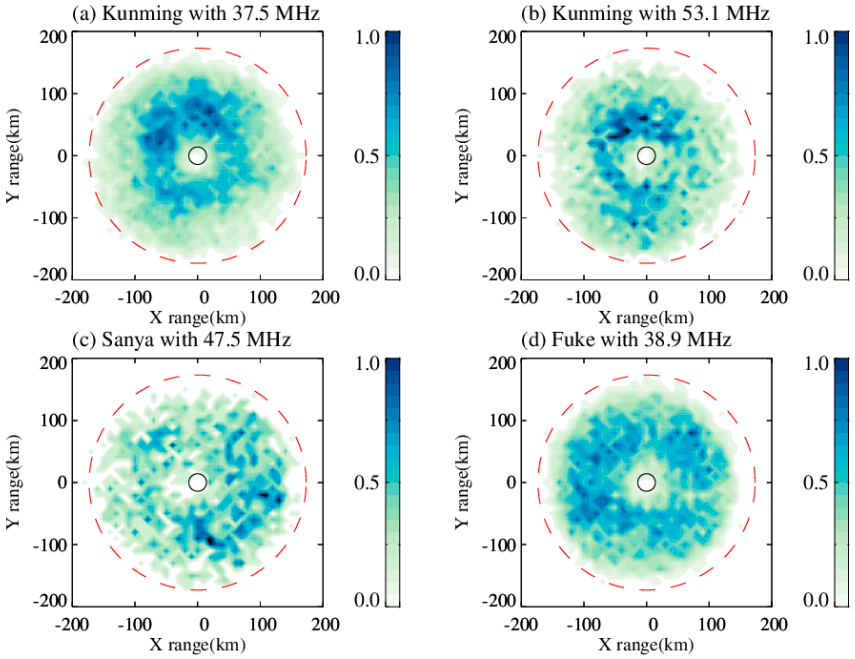

Figure A2. The normalized meteor counts observed by (**a**) the 37.5 MHz meteor radar, (**b**) the 53.1 MHz meteor radar, (**c**) the Sanya meteor radar, and (**d**) the Fuke meteor radar.

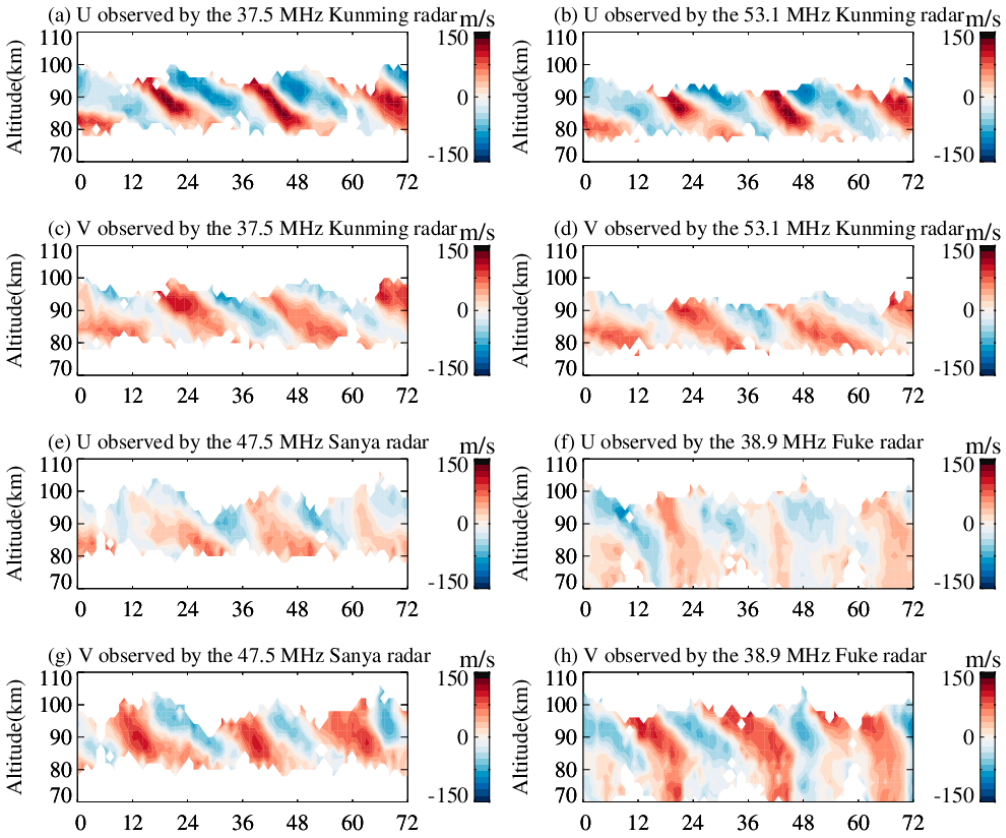

Figure A3. (**a**–**d**) Comparisons between the hourly zonal and meridional winds from 8 to 10 November 2013, observed by (**a**,**c**) the 37.5 MHz meteor radar and (**b**,**d**) the 53.1 MHz meteor radar. (**e**–**h**) Comparisons between the hourly zonal and meridional winds from 8 to 10 November 2015, observed by (**e**,**g**) the Sanya meteor radar and (**f**,**h**) the Fuke meteor radar.

References

1. Fritts, D.C.; Alexander, M.J. Gravity wave dynamics and effects in the middle atmosphere. *Rev. Geophys.* **2003**, *41*, 1003. [CrossRef]
2. Jia, M.; Xue, X.; Gu, S.; Chen, T.; Ning, B.; Wu, J.; Zeng, X.; Dou, X. Multiyear Observations of Gravity Wave Momentum Fluxes in the Midlatitude Mesosphere and Lower Thermosphere Region by Meteor Radar. *J. Geophys. Res.* **2018**, *123*, 5684–5703. [CrossRef]
3. Long, C.; Yu, T.; Sun, Y.-Y.; Yan, X.; Zhang, J.; Yang, N.; Wang, J.; Xia, C.; Liang, Y.; Ye, H. Atmospheric Gravity Wave Derived from the Neutral Wind with 5-Minute Resolution Routinely Retrieved by the Meteor Radar at Mohe. *Remote Sens.* **2023**, *15*, 296. [CrossRef]
4. Hedlin, M.A.H.; Drob, D.P. Statistical characterization of atmospheric gravity waves by seismoacoustic observations. *J. Geophys. Res. Atmos.* **2014**, *119*, 5345–5363. [CrossRef]
5. Zhang, G.; Xu, J.; Chen, X.; Sun, H.; Gong, L. Probing signals of atmospheric gravity waves excited by the 29 July 2021 MW8.2 Alaska earthquake. *Geod. Geodyn.* **2024**, *15*, 219–229. [CrossRef]
6. Lindzen, R.S. Turbulence and stress owing to gravity-wave and tidal breakdown. *J. Geophys. Res.* **1981**, *86*, 9707–9714. [CrossRef]
7. Vincent, R.A.; Reid, I. HF Doppler measurements of mesospheric gravity-wave momentum fluxes. *J. Atmos. Sci.* **1983**, *40*, 1321–1333. [CrossRef]
8. Ern, M.; Preusse, P.; Gille, J.C.; Hepplewhite, C.L.; Mlynczak, M.G.; Russell, J.M.; Riese, M. Implications for atmospheric dynamics derived from global observations of gravity wave momentum flux in stratosphere and mesosphere. *J. Geophys. Res.* **2011**, *116*, D19107. [CrossRef]
9. Hoffmann, L.; Xue, X.; Alexander, M.J. A global view of stratospheric gravity wave hotspots located with Atmospheric Infrared Sounder observations. *J. Geophys. Res. Atmos.* **2013**, *118*, 416–434. [CrossRef]
10. Liu, A.Z.; Lu, X.; Franke, S.J. Diurnal variation of gravity wave momentum flux and its forcing on the diurnal tide. *J. Geophys. Res. Atmos.* **2013**, *118*, 1668–1678. [CrossRef]
11. Zhou, B.; Xue, X.; Yi, W.; Ye, H.; Zeng, J.; Chen, J.; Wu, J.; Chen, T.; Dou, X. A comparison of MLT wind between meteor radar chain data and SD-WACCM results. *Earth Planet. Phys.* **2022**, *6*, 451–464. [CrossRef]
12. Wang, J.; Yi, W.; Wu, J.; Chen, T.; Xue, X.; Zeng, J.; Vincent, R.A.; Reid, I.; Batista, P.P.; Buriti, R.A.; et al. Coordinated observations of migrating tides by multiple meteor radars in the equatorial mesosphere and lower thermosphere. *J. Geophys. Res. Space Phys.* **2022**, *127*, e2022JA030678. [CrossRef]
13. Andrews, D.G.; Holton, J.R.; Leovy, C.B. *Middle Atmosphere Dynamics*; Academic Press: Cambridge, MA, USA, 1987. [CrossRef]
14. Holton, J.R. The role of gravity wave induced drag and diffusion in the momentum budget of the mesosphere. *J. Atmos. Sci.* **1982**, *39*, 791–799. [CrossRef]
15. Pramitha, M.; Kumar, K.K.; Ratnam, M.V.; Rao, S.V.B.; Ramkumar, G. Meteor Radar Estimations of Gravity Wave Momentum Fluxes: Evaluation Using Simulations and Observations Over Three Tropical Locations. *J. Geophys. Res. Space Phys.* **2019**, *124*, 7184–7201. [CrossRef]
16. De Wit, R.J.; Hibbins, R.E.; Espy, P.J. The seasonal cycle of gravity wave momentum flux and forcing in the high latitude northern hemisphere mesopause region. *J. Atmos. Sol.-Terr. Phys.* **2015**, *127*, 21–29. [CrossRef]
17. Geller, M.A.; Alexander, M.J.; Love, P.T.; Bacmeister, J.; Ern, M.; Hertzog, A.; Manzini, E.; Preusse, P.; Sato, K.; Scaife, A.; et al. A comparison between gravity wave momentum fluxes in observations and climate models. *J. Clim.* **2013**, *26*, 6383–6405. [CrossRef]
18. Voelker, G.S.; Bölöni, G.; Kim, Y.; Zängl, G.; Achatz, U. MS-GWaM: A 3-dimensional transient gravity wave parametrization for atmospheric models. *J. Atmos. Sci.* **2024**, *81*, 1181–1200. [CrossRef]
19. Kruse, C.G.; Richter, J.H.; Alexander, M.J.; Bacmeister, J.T.; Heale, C.; Wei, J. Gravity wave drag parameterizations for Earth's atmosphere. In *Fast Processes in Large-Scale Atmospheric Models: Progress, Challenges, and Opportunities*; Wiley: Hoboken, NJ, USA, 2023; pp. 229–256. [CrossRef]
20. Plougonven, R.; de la Cámara, A.; Hertzog, A.; Lott, F. How does knowledge of atmospheric gravity waves guide their parameterizations? *Q. J. R. Meteorol. Soc.* **2020**, *146*, 1529–1543. [CrossRef]
21. Jewtoukoff, V.; Hertzog, A.; Plougonven, R.; de la Cámara, A.; Lott, F. Gravity waves in the Southern Hemisphere derived from balloon observations and ECMWF analyses. *J. Atmos. Sci.* **2015**, *72*, 3449–3468. [CrossRef]
22. Placke, M.; Stober, G.; Jacobi, C. Gravity wave momentum fluxes in the MLT—Part I: Seasonal variation at Collm (51.3°N, 13.0°E). *J. Atmos. Sol.-Terr. Phys.* **2011**, *73*, 904–910. [CrossRef]
23. Fritts, D.C.; Janches, D.; Hocking, W.K.; Mitchell, N.J.; Taylor, M.J. Assessment of gravity wave momentum flux measurement capabilities by meteor radars having different transmitter power and antenna configurations. *J. Geophys. Res.* **2012**, *117*, D10108. [CrossRef]
24. Reichert, R.; Kaifler, B.; Kaifler, N.; Dörnbrack, A.; Rapp, M.; Hormaechea, J.L. High-Cadence Lidar Observations of Middle Atmospheric Temperature and Gravity Waves at the Southern Andes Hot Spot. *J. Geophys. Res. Atmos.* **2021**, *126*, e2021JD034683. [CrossRef]
25. Li, H.; Zhang, J.; Sheng, B.; Fan, Y.; Ji, X.; Li, Q. The Gravity Wave Activity during Two Recent QBO Disruptions Revealed by U.S. High-Resolution Radiosonde Data. *Remote Sens.* **2023**, *15*, 472. [CrossRef]
26. Leena, P.P.; Ratnam, M.V.; Murthy, B.K.; Rao, S. Detection of high frequency gravity waves using high resolution radiosonde observations. *J. Atmos. Sol.-Terr. Phys.* **2012**, *77*, 254–259. [CrossRef]

27. Pramitha, M.; Venkat Ratnam, M.; Leena, P.P.; Krishna Murthy, B.V.; Vijaya Bhaskar Rao, S. Identification of inertia gravity wave sources observed in the troposphere and the lower stratosphere over a tropical station Gadanki. *Atmos. Res.* **2016**, *176–177*, 202–211. [CrossRef]
28. Rapp, M.; Strelnikov, B.; Müllemann, A.; Lübken, F.J.; Fritts, D.C. Turbulence measurements and implications for gravity wave dissipation during the MaCWAVE/MIDAS rocket program. *Geophys. Res. Lett.* **2004**, *31*, L24S07. [CrossRef]
29. Vaughan, G.; Worthington, R.M. Inertia-gravity waves observed by the UK MST radar. *Q. J. R. Meteorol. Soc.* **2007**, *133*, 179–188. [CrossRef]
30. Andrioli, V.F.; Fritts, D.C.; Batista, P.P.; Clemesha, B.R. Improved analysis of all-sky meteor radar measurements of gravity wave variances and momentum fluxes. *Ann. Geophys.* **2013**, *31*, 889–908. [CrossRef]
31. Jia, M.; Xue, X.; Dou, X.; Tang, Y.; Yu, C.; Wu, J.; Xu, J.; Yang, G.; Ning, B.; Hoffmann, L. A case study of A mesoscale gravity wave in the MLT region using simultaneous multi-instruments in Beijing. *J. Atmos. Sol.-Terr. Phys.* **2016**, *140*, 1–9. [CrossRef]
32. Vincent, R.A.; Kovalam, S.; Reid, I.M.; Younger, J.P. Gravity wave flux retrievals using meteor radars. *Geophys. Res. Lett.* **2010**, *37*, L14802. [CrossRef]
33. Günzkofer, F.; Pokhotelov, D.; Stober, G.; Mann, I.; Vadas, S.L.; Becker, E.; Tjulin, A.; Kozlovsky, A.; Tsutsumi, M.; Gulbrandsen, N.; et al. Inferring neutral winds in the ionospheric transition region from atmospheric-gravity-wave traveling-ionospheric-disturbance (AGW-TID) observations with the EISCAT VHF radar and the Nordic Meteor Radar Cluster. *Ann. Geophys.* **2023**, *41*, 409–428. [CrossRef]
34. Qiao, Z.; Liu, A.Z.; Pedatella, N.M.; Stober, G.; Reid, I.M.; Fuentes, J.; Adami, C.L. Evidence for SSW Triggered Q6DW-Tide and Q6DW-Gravity Wave Interactions Observed by Meteor Radars at 30°S. *Geophys. Res. Lett.* **2024**, *51*, e2023GL108066. [CrossRef]
35. Whiteway, J.A.; Carswell, A.I. Lidar observations of gravity wave activity in the upper stratosphere over Toronto. *J. Geophys. Res.* **1995**, *100*, 14113–14124. [CrossRef]
36. Xue, X.H.; Sun, D.S.; Xia, H.Y.; Dou, X.K. Inertial gravity waves observed by a Doppler wind LiDAR and their possible sources. *Earth Planet. Phys.* **2020**, *4*, 461–471. [CrossRef]
37. Zhao, R.C.; Dou, X.K.; Sun, D.S.; Xue, X.H.; Zheng, J.; Han, Y.L.; Chen, T.D.; Wang, G.C.; Zhou, Y.J. Gravity waves observation of wind field in stratosphere based on a Rayleigh Doppler LiDAR. *Opt. Express* **2016**, *24*, A581–A591. [CrossRef]
38. Zhao, R.; Dou, X.; Xue, X.; Sun, D.; Han, Y.; Chen, C.; Zheng, J.; Li, Z.; Zhou, A.; Han, Y.; et al. Stratosphere and lower mesosphere wind observation and gravity wave activities of the wind field in China using a mobile Rayleigh Doppler lidar. *J. Geophys. Res. Space Phys.* **2017**, *122*, 8847–8857. [CrossRef]
39. Zhao, M.; Yu, Z.; Wang, H.; Li, M. Numerical optimization of auxiliary biaxial receiver to detect blind zone of pulsed coherent wind lidar. *Opt. Express* **2024**, *32*, 12800–12815. [CrossRef]
40. Shi, M.; Qiu, S.; Soon, W.; Herrera, V.M.V.; Xue, X.; Li, T.; Dou, X. Peculiar Wave Structure of the Mesospheric Sporadic Sodium Layer Observed by Lidars in Hefei (31.8°N, 117.3°E) and Wuhan (30.5°N, 114°E), Central China. *J. Geophys. Res. Atmos.* **2023**, *128*, e2023JD039111. [CrossRef]
41. Qiu, S.; Tang, Y.; Jia, M.; Xue, X.; Dou, X.; Li, T.; Wang, Y. A review of latitudinal characteristics of sporadic sodium layers, including new results from the Chinese Meridian Project. *Earth-Sci. Rev.* **2016**, *162*, 83–106. [CrossRef]
42. Qiu, S.; Shi, M.; Yousof, H.; Soon, W.; Jia, M.; Xue, X.; Li, T.; Ju, P.; Dou, X. Solitary wave characteristics on the fine structure of the mesospheric sporadic sodium layer. *Front. Astron. Space Sci.* **2023**, *10*, 1241663. [CrossRef]
43. Salinas, C.C.J.H.; Wu, D.L.; Lee, J.N.; Chang, L.C.; Qian, L.; Liu, H. Aura/MLS observes and SD-WACCM-X simulates the seasonality, quasi-biennial oscillation and El Niño–Southern Oscillation of the migrating diurnal tide driving upper mesospheric CO primarily through vertical advection. *Atmos. Chem. Phys.* **2023**, *23*, 1705–1730. [CrossRef]
44. Ern, M.; Ploeger, F.; Preusse, P.; Gille, J.C.; Gray, L.J.; Kalisch, S.; Mlynczak, M.G.; Russell III, J.M.; Riese, M. Interaction of gravity waves with the QBO: A satellite perspective. *J. Geo-Phys. Res. Atmos.* **2014**, *119*, 2329–2355. [CrossRef]
45. Qiu, S.; Wang, N.; Soon, W.; Herrera, V.M.V.; Yang, C.; Dou, X. The Hemispheric Asymmetry of Gravity Wave Impact on the Polar Mesospheric Cloud, Based on the Aeronomy of Ice in the Mesosphere Satellite. *Atmosphere* **2023**, *14*, 419. [CrossRef]
46. Taori, A.; Jayaraman, A.; Kamalakar, V. Imaging of mesosphere–thermosphere airglow emissions over Gadanki (13.5°N, 79.2°E)—First results. *J. Atmos. Sol.-Terr. Phys.* **2013**, *93*, 21–28. [CrossRef]
47. Tang, Y.; Dou, X.; Li, T.; Nakamura, T.; Xue, X.; Huang, C.; Manson, A.; Meek, C.; Thorsen, D.; Avery, S. Gravity wave characteristics in the mesopause region revealed from OH airglow imager observations over Northern Colorado. *J. Geophys. Res. Space Phys.* **2014**, *119*, 630–645. [CrossRef]
48. Wei, Y.; Gu, S.Y.; Li, N.; Qin, Y.; Sun, R.; Wang, D.; Hu, G.; Le, H.; Yuan, W. Passive optical observation of mesosphere and thermosphere wind over three stations in China. *J. Geophys. Res. Space Phys.* **2023**, *129*, e2023JA032214. [CrossRef]
49. Wei, Y.; Gu, S.; Sun, R.; Huang, C. Correction of distorted FPI interferograms to invert atmospheric winds and temperatures. *Opt. Express* **2023**, *31*, 19404–19414. [CrossRef]
50. Hocking, W.K. A new approach to momentum flux determinations using SKiYMET meteor radars. *Ann. Geophys.* **2005**, *23*, 2433–2439. [CrossRef]
51. Placke, M.; Hoffmann, P.; Latteck, R.; Rapp, M. Gravity wave momentum fluxes from MF and meteor radar measurements in the polar MLT region. *J. Geophys. Res. Space Phys.* **2015**, *120*, 736–750. [CrossRef]
52. Andrioli, V.F.; Batista, P.P.; Clemesha, B.R.; Schuch, N.J.; Buriti, R.A. Multi-year observations of gravity wave momentum fluxes at low and middle latitudes inferred by all-sky meteor radar. *Ann. Geophys.* **2015**, *33*, 1183–1193. [CrossRef]

53. de Wit, R.J.; Janches, D.; Fritts, D.C.; Hibbins, R.E. QBO modulation of the mesopause gravity wave momentum flux over Tierra del Fuego. *Geophys. Res. Lett.* **2016**, *43*, 4049–4055. [CrossRef]
54. de Wit, R.J.; Janches, D.; Fritts, D.C.; Stockwell, R.G.; Coy, L. Unexpected climatological behavior of MLT gravity wave momentum flux in the lee of the Southern Andes hot spot. *Geophys. Res. Lett.* **2017**, *44*, 1182–1191. [CrossRef]
55. Moss, A.C.; Wright, C.J.; Davis, R.N.; Mitchell, N.J. Gravity-wave momentum fluxes in the mesosphere over Ascension Island (8°S, 14°W) and the anomalous zonal winds of the semi-annual oscillation in 2002. *Ann. Geophys.* **2016**, *34*, 323–330. [CrossRef]
56. Li, G.; Ning, B.; Li, A.; Yang, S.; Zhao, X.; Zhao, B.; Wan, W. First results of optical meteor and meteor trail irregularity from simultaneous Sanya radar and video observations. *Earth Planet. Phys.* **2018**, *2*, 15–21. [CrossRef]
57. Holdsworth, D.A.; Reid, I.M.; Cervera, M.A. Buckland Park all-sky interferometric meteor radar. *Radio Sci.* **2004**, *39*, 12. [CrossRef]
58. Yi, W.; Xue, X.; Reid, I.M.; Murphy, D.; Hall, C.; Tsutsumi, M.; Ning, B.; Li, G.; Vincent, R.A.; Chen, J.; et al. Climatology of the mesopause relative density using a global distribution of meteor radars. *Atmos. Chem. Phys.* **2019**, *19*, 7567–7581. [CrossRef]
59. Zeng, J.; Stober, G.; Yi, W.; Xue, X.; Zhong, W.; Reid, I.; Adami, C.L.; Ning, B.; Li, G.; Dou, X. Mesosphere/lower thermosphere 3-dimensional spatially resolved winds observed by Chinese multistatic meteor radar network using the newly developed VVP method. *J. Geophys. Res. Atmos.* **2024**, *129*, e2023JD040642. [CrossRef]
60. Li, J.; Yi, W.; Xue, X.H.; Zeng, J.; Ye, H.L.; Wang, J.Y.; Chen, J.S.; Li, N.; Chen, T.D. Mesospheric tide comparisons at low latitudes observed by two collocated meteor radars. *Earth Planet. Phys.* **2024**, *8*, 1–15. [CrossRef]
61. Yi, W.; Xue, X.; Reid, I.; Murphy, D.; Hall, C.; Tsutsumi, M.; Ning, B.; Li, G.; Yang, G.; Li, N.; et al. Climatology of interhemispheric mesopause temperatures using the high-latitude and middle-latitude meteor radars. *J. Geophys. Res. Atmos.* **2021**, *126*, e2020JD034301. [CrossRef]
62. Yang, C.; Lai, D.; Yi, W.; Wu, J.; Xue, X.; Li, T.; Chen, T.; Dou, X. Observed Quasi 16-Day Wave by Meteor Radar over 9 Years at Mengcheng (33.4°N, 116.5°E) and Comparison with the Whole Atmosphere Community Climate Model Simulation. *Remote Sens.* **2023**, *15*, 830. [CrossRef]
63. Zeng, J.; Yi, W.; Xue, X.; Reid, I.; Hao, X.; Li, N.; Chen, J.; Chen, T.; Dou, X. Comparison between the Mesospheric Winds Observed by Two Collocated Meteor Radars at Low Latitudes. *Remote Sens.* **2022**, *14*, 2354. [CrossRef]
64. Yi, W.; Xue, X.; Chen, J.; Chen, T.; Li, N. Quasi-90-day oscillation observed in the MLT region at low latitudes from the Kunming meteor radar and SABER. *Earth Planet. Phys.* **2019**, *3*, 136–146. [CrossRef]
65. Yi, W.; Xue, X.; Reid, I.; Younger, J.P.; Chen, J.; Chen, T.; Li, N. Estimation of mesospheric densities at low latitudes using the Kunming meteor radar together with SABER temperatures. *J. Geophys. Res. Space Phys.* **2018**, *123*, 3183–3195. [CrossRef]
66. Yi, W.; Xue, X.; Chen, J.; Dou, X.; Chen, T.; Li, N. Estimation of mesopause temperatures at low latitudes using the Kunming meteor radar. *Radio Sci.* **2016**, *51*, 130–141. [CrossRef]
67. Hocking, W.K.; Fuller, B.; Vandepeer, B. Real-time determination of meteor-related parameters utilizing modem digital technology. *J. Atmos. Sol.-Terr. Phys.* **2001**, *63*, 155–169. [CrossRef]
68. Hersbach, H.; Dee, D. ERA5 reanalysis is in production, ECMWF Newsletter 147, ECMWF, Reading, UK. 2016. Available online: https://www.ecmwf.int/en/newsletter/147/news/era5-reanalysis-production (accessed on 25 May 2024).
69. Hersbach, H.; Bell, B.; Berrisford, P.; Hirahara, S.; Horanyi, A.; Munoz-Sabater, J.; Nicolas, J.; Peubey, C.; Radu, R.; Schepers, D.; et al. The ERA5 global reanalysis. *Q. J. R. Meteorol. Soc.* **2020**, *146*, 1999–2049. [CrossRef]
70. Gruber, A.; Winston, J.S. Earth-atmosphere radiative heating based on NOAA scanning radiometer measurements. *Bull. Am. Meteorol. Soc.* **1978**, *59*, 1570–1573. [CrossRef]
71. Zhong, W.; Xue, X.; Yi, W.; Reid, I.M.; Chen, T.; Dou, X. Error analyses of a multistatic meteor radar system to obtain a three-dimensional spatial-resolution distribution. *Atmos. Meas. Tech.* **2021**, *14*, 3973–3988. [CrossRef]
72. Li, N.; Chen, J.; Ding, Z.; Zhao, L. Study on the characteristics of atmospheric waves in near space during 2013 stratosphere sudden warming in Kunming, China. *Chin. J. Radio Sci.* **2023**, *38*, 679–685.
73. Li, N.; Chen, J.; Wang, J.; Zhao, L.; Ding, Z.; He, G. Oscillations of GW Activities in the MLT Region over Mid-Low-Latitude Area, Kunming Station (25.6° N, 103.8° E). *Atmosphere* **2023**, *14*, 1810. [CrossRef]
74. Gupta, A.; Birner, T.; Dörnbrack, A.; Polichtchouk, I. Importance of Gravity Wave Forcing for Springtime Southern Polar Vortex Breakdown as Revealed by ERA5. *Geophys. Res. Lett.* **2021**, *48*, e2021GL092762. [CrossRef]
75. Ma, Z.; Gong, Y.; Zhang, S.; Zhou, Q.; Huang, C.; Huang, K.; Dong, W.; Li, G.; Ning, B. Study of Mean Wind Variations and Gravity Wave Forcing Via a Meteor Radar Chain and Comparison with HWM-07 Results. *J. Geophys. Res. Atmos.* **2018**, *123*, 9488–9501. [CrossRef]
76. Gong, S.; Yang, G.; Xu, J.; Liu, X.; Li, Q. Gravity Wave Propagation from the Stratosphere into the Mesosphere Studied with Lidar, Meteor Radar, and TIMED/SABER. *Atmosphere* **2019**, *10*, 81. [CrossRef]
77. Li, Q.; Xu, J.; Yue, J.; Yuan, W.; Liu, X. Statistical characteristics of gravity wave activities observed by an OH airglow imager at Xinglong, in northern China. *Ann. Geophys.* **2011**, *29*, 1401–1410. [CrossRef]
78. Li, Q.; Xu, J.; Liu, X.; Yuan, W.; Chen, J. Characteristics of mesospheric gravity waves over the southeastern Tibetan Plateau region. *J. Geophys. Res. Space Phys.* **2016**, *121*, 9204–9221. [CrossRef]
79. Liu, H.-L.; Marsh, D.R.; She, C.-Y.; Wu, Q.; Xu, J. Momentum balance and gravity wave forcing in the mesosphere and lower thermosphere. *Geophys. Res. Lett.* **2009**, *36*, L07805. [CrossRef]
80. Li, R.; Xu, X.; Wang, Y.; Teixeira, M.A.C.; Tang, J.; Xu, Y. The Response of Parameterized Orographic Gravity Waves to Rapid Warming over the Tibetan Plateau. *Atmosphere* **2020**, *11*, 1016. [CrossRef]

81. Xu, J.; Li, Q.; Yue, J.; Hoffmann, L.; Straka, W.C., III; Wang, C.; Liu, M.; Yuan, W.; Han, S.; Miller, S.D.; et al. Concentric gravity waves over northern China observed by an airglow imager network and satellites. *J. Geophys. Res. Atmos.* **2015**, *120*, 11058–11078. [CrossRef]
82. Hitchman, M.H.; Bywaters, K.W.; Fritts, D.C.; Coy, L.; Kudeki, E.; Surucu, F. Mean winds and momentum fluxes over Jicamarca, Peru, during June and August 1987. *J. Atmos. Sci.* **1992**, *49*, 2372–2383. [CrossRef]
83. Reid, I.; Vincent, R.A. Measurements of mesospheric gravity wave momentum fluxes and mean flow accelerations at Adelaide, Australia. *J. Atmos. Terr. Phys.* **1987**, *49*, 443–460. [CrossRef]